INORGANIC CHEMISTRY FRONTIERS

RESEARCH ARTICLE

View Article Online
View Journal | View Issue

Check for updates

Cite this: *Inorg. Chem. Front.*, 2026, **13**, 4031

Single-component zero-dimensional $(BPY)_2ZrCl_6$:Sb^{3+} hybrid perovskite exhibiting excitation-dependent multi-color fluorescence and afterglow for advanced hierarchical anti-counterfeiting

Qi Chen,[a] Chenyang Zhang,[a] Hu Wang,[a] Yuexiao Pan,*[a] Hongzhou Lian,[b] Jun Lin*[b] and Liyi Li*[c]

Received 14th December 2025,
Accepted 5th March 2026

DOI: 10.1039/d5qi02511g

rsc.li/frontiers-inorganic

Single-component materials capable of exhibiting both excitation-dependent fluorescence and time-resolved afterglow are highly desirable for advanced photonic applications, yet remain scarce. Herein, we report a novel zero-dimensional (0D) organic–inorganic hybrid perovskite (OIHP), $(BPY)_2ZrCl_6$:Sb^{3+}([BPY]$^+$ = *N*-butyl-pyridinium cation), which exhibits excitation-dependent fluorescence and green afterglow properties. This dual emission originates from distinct luminescent centers: self-trapped excitons (STEs) and d–d transitions within the $[ZrCl_6]^{2-}$ octahedra, and the organic $[BPY]^+$ cations. The incorporation of Sb^{3+} enables efficient energy transfer from the host to the $[SbCl_6]^{3-}$ dopant, leading to broadly tunable white-light emission from green to orange-red and a notable reduction in afterglow lifetime. Density functional theory calculations revealed the origin of the afterglow, and the band narrowing and exciton localization effects caused by Sb^{3+} doping. Leveraging this tunable emission and time-resolved afterglow, we demonstrate high-quality white light-emitting diodes (WLEDs) and a dynamic anti-counterfeiting system using ASCII-based time-gated decoding. This work provides insights into energy-transfer engineering in 0D OIHP and establishes a material platform that integrates efficient lighting with advanced information encryption.

Published on 18 März 2026. Downloaded on 05.06.2026 21:27:24.

1. Introduction

In the era of the digital economy, information forgery and data leakage pose severe threats to global economic security, creating a pressing need for efficient and multi-level information encryption and anti-counterfeiting technologies.[1–4] Conventional anti-counterfeiting methods based on static patterns or single-mode luminescence are vulnerable to replication and thus insufficient for high-security applications.[5,6] In recent years, luminescent materials with time-resolved characteristics, particularly long-persistent luminescence and room-temperature phosphorescence (RTP) materials, have introduced a temporal dimension, offering new pathways for dynamic and multi-level information encryption.[7–11] However, progress in this field remains constrained by material performance. Achieving a high-performance, multimodal, and easily integrated luminescent system represents an ongoing challenge.

Inorganic long-persistent luminescence materials such as $SrAl_2O_4$:Eu^{2+}, Dy^{3+} and $MgGa_2O_4$:Bi^{3+}, though known for their long afterglow duration and high brightness, typically require high-temperature solid-state synthesis, which is energy-intensive and environmentally harmful.[12,13] Organic RTP systems circumvent the sintering problem through host–guest doping and polymer-matrix encapsulation, however, multi-component blends inevitably suffer from aggregation-caused quenching, spectral cross-talk, and phase separation after thermal cycling or long-term irradiation, which deteriorate the reliability of hidden codes.[14–18] In contrast, single-component luminescent materials offer distinct advantages by avoiding issues such as energy reabsorption and phase separation inherent in multi-phase systems.

0D OIHP are composed of isolated metal–halide octahedra surrounded by bulky organic cations have recently emerged as

[a]*Key Laboratory of Carbon Materials of Zhejiang Province, College of Chemistry and Materials Engineering, Wenzhou University, Wenzhou 325035, P.R. China. E-mail: yxpan@wzu.edu.cn*
[b]*Key Laboratory of Rare Earth Resource Utilization, Changchun Institute of Applied Chemistry, Chinese Academy of Sciences, Changchun 130022, P. R. China. E-mail: jlin@ciac.ac.cn*
[c]*Research Center for Eco-environmental Engineering, Dongguan University of Technology, Dongguan, 523808, P. R. China. E-mail: liliyi@dgut.edu.cn*

Published on 18 März 2026. Downloaded on 05.06.2026 21:27:24.

a unique platform that unites the structural rigidity of inorganic lattices with the chemical versatility of organic moieties.[19–21] For instance, $(Ph_4P)_2Cd_2Br_6$ exhibits ultra-long RTP that is thermally stable from 100 to 320 K, validating the ability of inorganic cages to immobilize triplet excitons.[20] Nevertheless, most studies optimize only one optical parameter, and a single-phase OIHP that delivers both excitation-dependent multi-color fluorescence and time-dependent afterglow has not been realized.

Doping ns^2 metal ions whose lone-pair s electrons strongly couple with lattice phonons has recently been identified as an efficient route to engineer STEs and create multiple emissive centers within one crystal.[22–26] Representative works include $(ETPP)_2ZrCl_6:Te^{4+}$ that enables reversible fluorescence-phosphorescence switching and $(Ph_3S)_2SnCl_6:Sb^{3+}/Bi^{3+}$ that establishes cascaded energy funnels from singlet/triplet states to STEs, producing dual-mode emission for time-dependent encryption.[22,23] These proofs of concept highlight the feasibility of exploiting ns^2 dopants to manipulate energy transfer pathways. However, systematic integration of temporal code multiplexing with solid-state lighting, especially high-color-rendering WLEDs, has rarely been demonstrated.

In this work, we present a novel single-component 0D OIHP, $(BPY)_2ZrCl_6:Sb^{3+}$, that simultaneously exhibits excitation-wavelength-tunable fluorescence spanning green to orange-red and green afterglow. DFT calculations and related spectroscopic analyses reveal an unusual stepwise energy transfer pathway: from the organic cation $[BPY]^+$ to the inorganic $[ZrCl_6]^{2-}$ octahedra, and further to the $[SbCl_6]^{3-}$ units. This cascade process effectively funnels excitation energy through the system and suppresses non-radiative losses, leading to the high overall emission efficiency. Our work not only advances the fundamental understanding of exciton dynamics in doped 0D perovskite, but also provides a ready-to-use material platform that bridges high-security information protection and energy-efficient solid-state lighting.

2. Results and discussion

2.1. Structural of Sb^{3+} incorporation into 0D $(BPY)_2ZrCl_6$

Hydrothermal treatment of *N*-butyl-pyridinium chloride BPYCl and $ZrCl_4$ in concentrated HCl yielded colorless plate-like single crystals of $(BPY)_2ZrCl_6$ (Fig. S1). Single-crystal X-ray diffraction performed at 296 K confirmed the expected 0D motif in which isolated $[ZrCl_6]^{2-}$ octahedra are spatially separated by $[BPY]^+$ cations (Fig. 1a and b). The structure was refined in the monoclinic space group $P2_1/c$ with cell parameters a = 15.0154 Å, b = 16.4714 Å, c = 10.4913 Å, $\alpha = \gamma = 90°$, and β = 90.020° (Table S1). The Zr–Cl bond lengths range from 2.433 to 2.465 Å, consistent with expected values and indicating a slightly distorted octahedral environment.[27] The crystallographic data have been deposited at the Cambridge Crystallographic Data Center (CCDC #2454281).

The powder X-ray diffraction (PXRD) patterns of $(BPY)_2ZrCl_6:x\%Sb^{3+}$ (x = 0–45) samples indicate pure phases with high crystallinity (Fig. 1c). The diffraction peaks gradually shift to lower angles. This shift occurs because the ionic radius of Sb^{3+} (r = 0.76 Å) is larger than that of Zr^{4+} (r = 0.72 Å), the partial substitution thus leads to lattice expansion.[28,29] Fig. S2 shows the Rietveld refinement of the PXRD pattern for $(BPY)_2ZrCl_6:Sb^{3+}$. Table S2 shows the lattice parameters (a, b, c axes) obtained from Rietveld refinement. The results show only slight changes in cell parameters and confirm the absence of impurity phases. Fourier-transform infrared (FTIR) spectra of BPYCl, $(BPY)_2ZrCl_6$, and $(BPY)_2ZrCl_6:Sb^{3+}$ are superimposable in the 2869–3006 cm^{-1} (νC–H), 1632 cm^{-1} (νC=N), 1490 cm^{-1} (νC=C), 1170 cm^{-1} (νC–N), and 698–805 cm^{-1} (δC–Cl) regions (Fig. 1d), indicating that the organic cation remains chemically intact upon doping.

X-ray photoelectron spectroscopy (XPS) was used to probe the electronic environment after substitution. Survey spectra (Fig. 1e) exhibited signals from C, N, Zr, Cl, and Sb without detectable impurities. High-resolution scans (Fig. 1f–h) revealed Zr $3d_{3/2}$ and $3d_{5/2}$ peaks at 184.6 and 182.4 eV, respectively, and Cl $2p_{1/2}$ and $2p_{3/2}$ peaks at 199.4 and 197.8 eV, upon Sb^{3+} introduction, both Zr 3d and Cl 2p envelopes shifted toward higher binding energy, signifying a small decrease in electron density on the $[ZrCl_6]^{2-}$ moiety. Simultaneously, spin–orbit-split Sb $3d_{3/2}$ (539.8 eV) and $3d_{5/2}$ (530.9 eV) doublets confirmed Sb has +3 state.[30]

2.2. Optical properties, afterglow color, and triplet-to-STEs energy transfer in Sb^{3+}-doped 0D $(BPY)_2ZrCl_6$

To elucidate the emission properties of $(BPY)_2ZrCl_6$, its photoluminescence excitation (PLE) and photoluminescence (PL) spectra were collected. Under 304 nm excitation, a broad emission band spanning 350 to 700 nm with a full width at half maximum (FWHM) of 182 nm was observed (Fig. S3), which is characteristic of STEs localized within the $[ZrCl_6]^{2-}$ octahedra.[31–33] Five discrete emission peaks located at 466, 500, 523, 547, and 573 nm were resolved; the four longer-wavelength features became significantly sharper at 77 K (Fig. S4) as non-radiative pathways were suppressed. The 466 nm peak was attributed to the $\pi^* \rightarrow$ n transition of the BPYCl, whereas 500, 523, 547, and 573 nm manifold was assigned to $^1F_3 \rightarrow {}^3F_2$, $^3D_3 \rightarrow {}^3F_4$, $^3D_2 \rightarrow {}^3F_2$, and $^3D_3 \rightarrow {}^3P_2$ d–d transitions of Zr (IV) in a distorted octahedral field.[27,34,35] This assignment was corroborated by independent measurements of BPYCl, which exhibited excitation maxima at 326 and 355 nm and an emission peak at 466 nm (Fig. S5). Excitation spectra monitored at the different emission wavelengths provide further evidence: those monitored at 500, 523, 547, and 573 nm are superimposable, whereas the spectrum monitored at 466 nm is distinct (Fig. S6). This confirms that the longer-wavelength emissions share a common origin from the $[ZrCl_6]^{2-}$ center, while the 466 nm emission arises from the organic cation. Armed with this dual-center picture, a concentration series of Sb^{3+} was introduced into the lattice to investigate energy-transfer-driven spectral tuning.

Optical photographs recorded under 340 nm irradiation revealed a systematic color evolution from green to orange-red

 This journal is © the Partner Organisations 2026

Published on 18 März 2026. Downloaded on 05.06.2026 21:27:24.

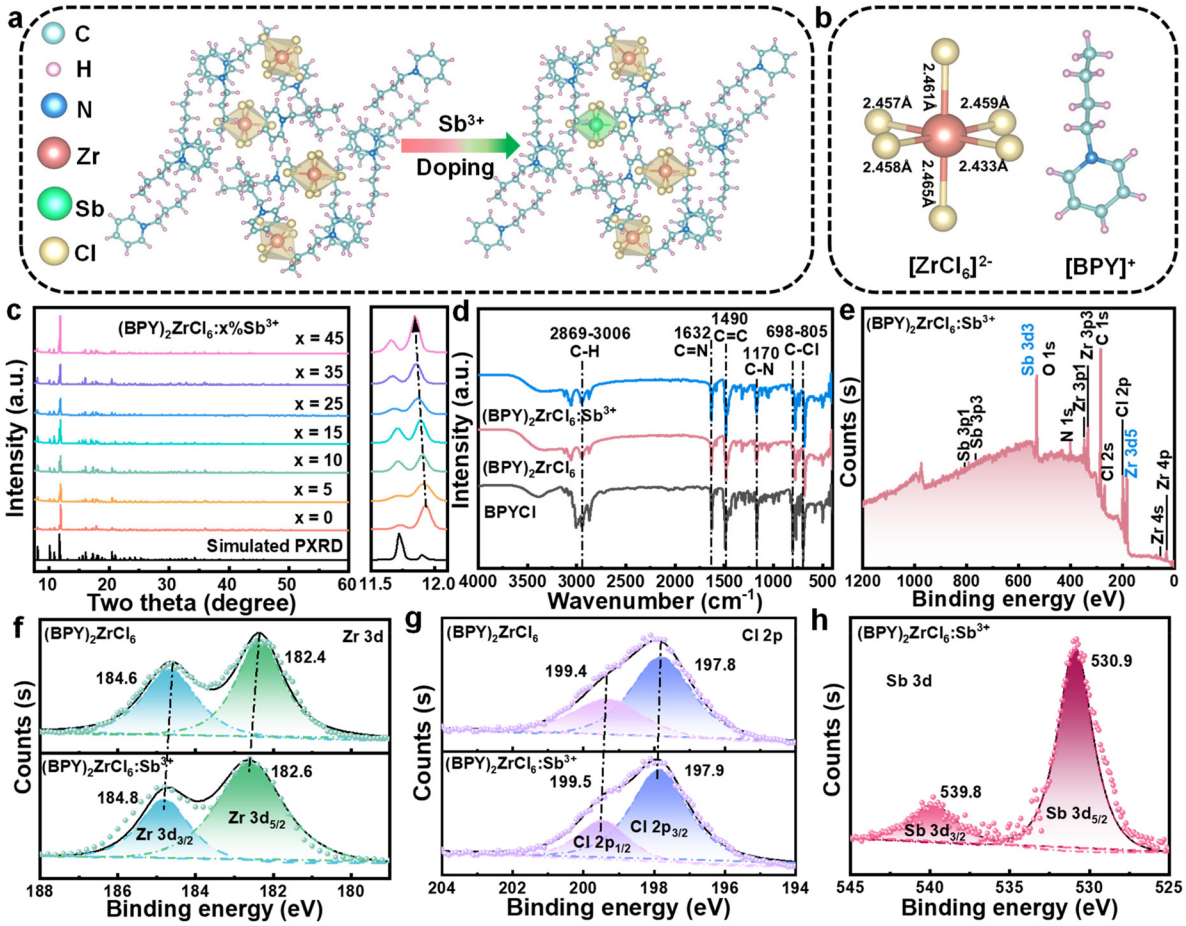

Fig. 1 (a) 0D $(BPY)_2ZrCl_6$ framework and Sb^{3+} doping scheme. (b) Ball-and-stick diagram of individual $[ZrCl_6]^{2-}$ unit and organic cation $[BPY]^+$. (c) PXRD patterns of $(BPY)_2ZrCl_6$:Sb^{3+} with different Sb^{3+} doping concentrations. (d) FTIR spectra of BPYCl, $(BPY)_2ZrCl_6$ and $(BPY)_2ZrCl_6$:Sb^{3+}. (e) XPS survey spectra of $(BPY)_2ZrCl_6$:Sb^{3+}. High-resolution XPS spectra of (f) Zr 3d, (g) Cl 2p, and (h) Sb 3d for $(BPY)_2ZrCl_6$ and $(BPY)_2ZrCl_6$:Sb^{3+}.

as the Sb^{3+} fraction was increased from 0 to 45% (Fig. 2a). Excitation spectra were acquired while monitoring the intrinsic 500 nm and the dopant-related 616 nm emissions (Fig. 2b and c). The intensity at 500 nm decreased monotonically with increasing Sb^{3+} content, while that at 616 nm showed the opposite trend up to 35%Sb^{3+}, beyond which it drops. This antiphase behavior is consistent with a donor–acceptor energy transfer pathway in which the $[ZrCl_6]^{2-}$ octahedron serves as the primary photon absorber and subsequently funnels excitation energy into the $[SbCl_6]^{3-}$ trap. The subsequent decline of the 616 nm excitation intensity beyond 35%Sb^{3+} is attributed to concentration quenching, whereby enhanced non-radiative cross-relaxation between neighboring $[SbCl_6]^{3-}$ units deactivates the emitting state and lowers the overall transfer efficiency.[36,37] Upon 304 nm excitation the 500 nm band was found to decrease continuously with increasing Sb^{3+} content, whereas the 616 nm emission first intensified as the dopant level rose from 0 to 35% and then declined at 45% (Fig. 2d), a behavior ascribed to concentration quenching.[38] Under 340 nm pumping the 500 nm peak exhibited a 20 nm blue-shift relative to the 304 nm data (Fig. S7), indicating a larger contribution from the organic BPYCl center. Nevertheless, the 480 nm intensity still decreased monotonically while the 616 nm band followed the same rise-and-fall pattern (Fig. 2e), confirming that the energy transfer scenario is independent of the primary excitation wavelength. This scenario is further supported by low-temperature PL spectra at 77 K (Fig. S8), which reveal that the well-resolved d-d transition peaks of the host are progressively suppressed upon Sb^{3+} doping, while the dopant's STEs emission intensifies. Analysis of the Commission International d'Eclairage (CIE) chromaticity (Fig. S9) coordinates from the PL spectra confirms that the emission color shifts progressively from green to orange-red as the Sb^{3+} concentration increases, underlining the continuous and excitation-dependent color tenability.

Time-resolved measurements provided quantitative evidence for the proposed donor–acceptor pathway. The fluorescence lifetime of the matrix $(BPY)_2ZrCl_6$ at 500 nm was 16.18 μs. Upon doping with different concentrations of Sb^{3+}, the fluorescence lifetime decreased from 15.32 μs to 9.94 μs at 500 nm, and from 9.10 μs to 6.44 μs at 616 nm. The decrease in the fluorescence lifetime of Sb^{3+} emission at 616 nm further

Published on 18 März 2026. Downloaded on 05.06.2026 21:27:24.

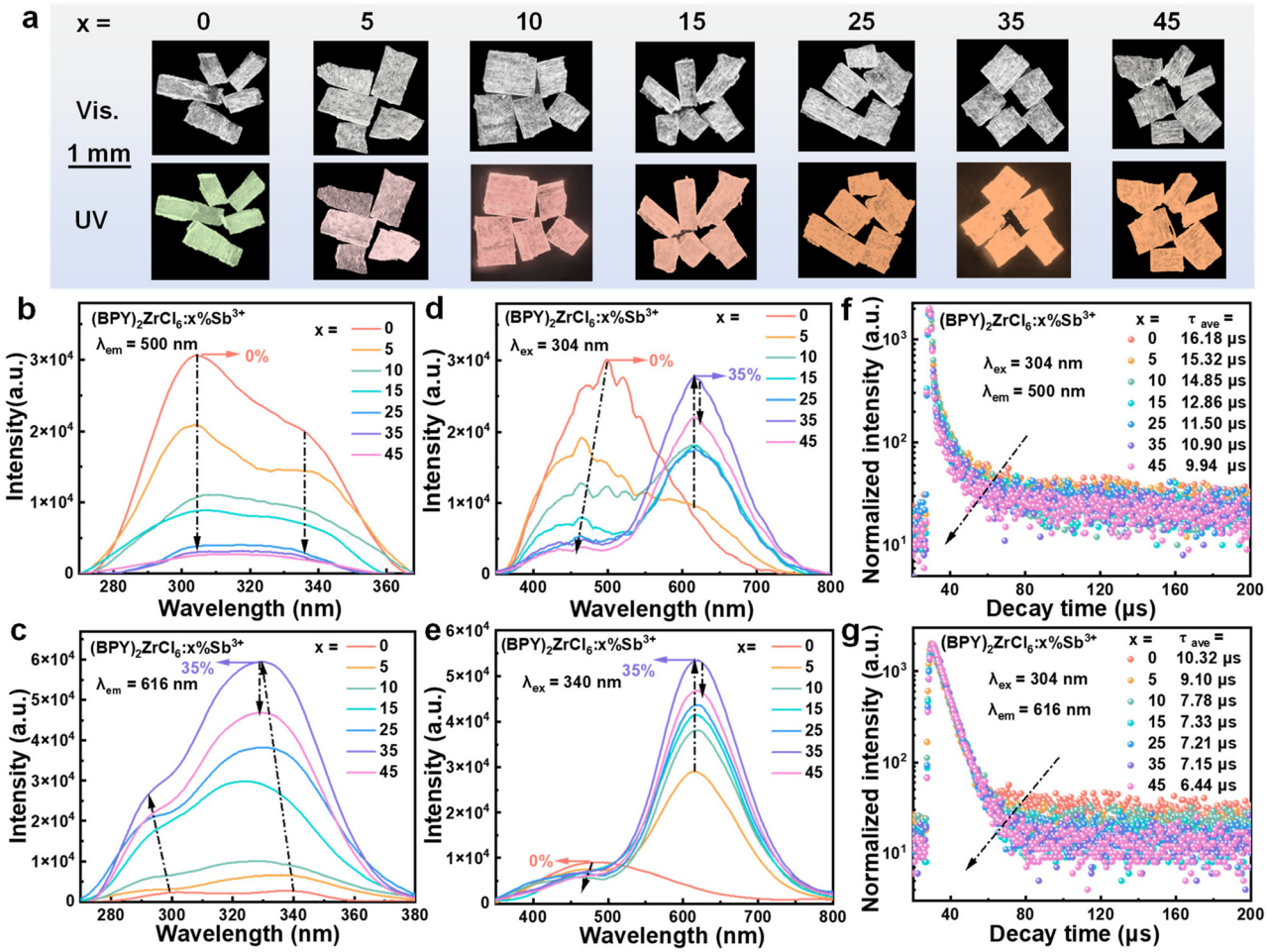

Fig. 2 (a) Photographs of $(BPY)_2ZrCl_6$:x%Sb^{3+} (*x* = 0–45) crystals taken under visible and 340 nm UV lights. (b and c) PLE spectra of $(BPY)_2ZrCl_6$:x%Sb^{3+} (*x* = 0–45) monitored at 500 nm and 616 nm. (d and e) PL spectra of $(BPY)_2ZrCl_6$:x%Sb^{3+} (*x* = 0–45) excited at 304 nm and 340 nm. (f and g) Decay curves spectra of $(BPY)_2ZrCl_6$:x%Sb^{3+} (*x* = 0–45).

confirms the efficient energy transfer process from $[ZrCl_6]^{2-}$ STEs to $[SbCl_6]^{3-}$ traps (Fig. 2f and g). The energy transfer efficiency (η_{ET}) can be obtained using the following equation:[39,40]

$$\eta_{\tau_{ET}} = 1 - \tau_{S/}\tau_{S0} \quad (1)$$

τ_S and τ_{S0} respectively represent the lifetimes when Sb^{3+} ions are present and absent. As shown in Fig. S10, as the concentration of Sb^{3+} ions increases, the energy transfer efficiency rises from 5.32% to 38.57%. Photoluminescence quantum yields (PLQYs) measurements revealed a pronounced enhancement from the host value of 8.28% to 83.21% at 35%Sb^{3+}, followed by a decrease to 66.26% at 45%Sb^{3+} (Fig. S11 and S12). The close correspondence between PLQYs and emission-intensity trends (Fig. S13) demonstrates that the energy transfer process not only redistributes spectral weight but also suppresses non-radiative losses, thereby enabling single-component white-light generation with PLQYs of 83.21% for Sb^{3+}-doped 0D hybrid halides.

Interestingly, in addition to having notable fluorescence emission properties, the $(BPY)_2ZrCl_6$ crystal also exhibits good afterglow emission performance. When the undoped $(BPY)_2ZrCl_6$ host was monitored at 500 nm under delayed conditions, a single prominent excitation peak centered at 295 nm was recorded (Fig. 3a). Illumination at this wavelength yielded the corresponding delayed emission spectrum (Fig. 3b), in which a narrow band at 466 nm was observed that perfectly matches the afterglow maximum for crystalline BPYCl (Fig. S14). In addition, four equally well-resolved maxima appeared at 500, 523, 547, and 573 nm, *i.e.* at the same positions already detected in the prompt fluorescence spectrum and therefore unambiguously derived from the octahedral $[ZrCl_6]^{2-}$. To corroborate these individual attributions, delayed excitation spectra were acquired while successively fixing the detection window at 466, 500, 523, 547, and 573 nm (Fig. S15). The traces recorded at 500, 523, 547, and 573 nm are superimposable, whereas the 466 nm channel exhibits an excitation maximum that is blue-shifted by 7 nm and displays a subtly different lineshape, thereby confirming that the 466 nm emis-

 This journal is © the Partner Organisations 2026

Published on 18 März 2026. Downloaded on 05.06.2026 21:27:24.

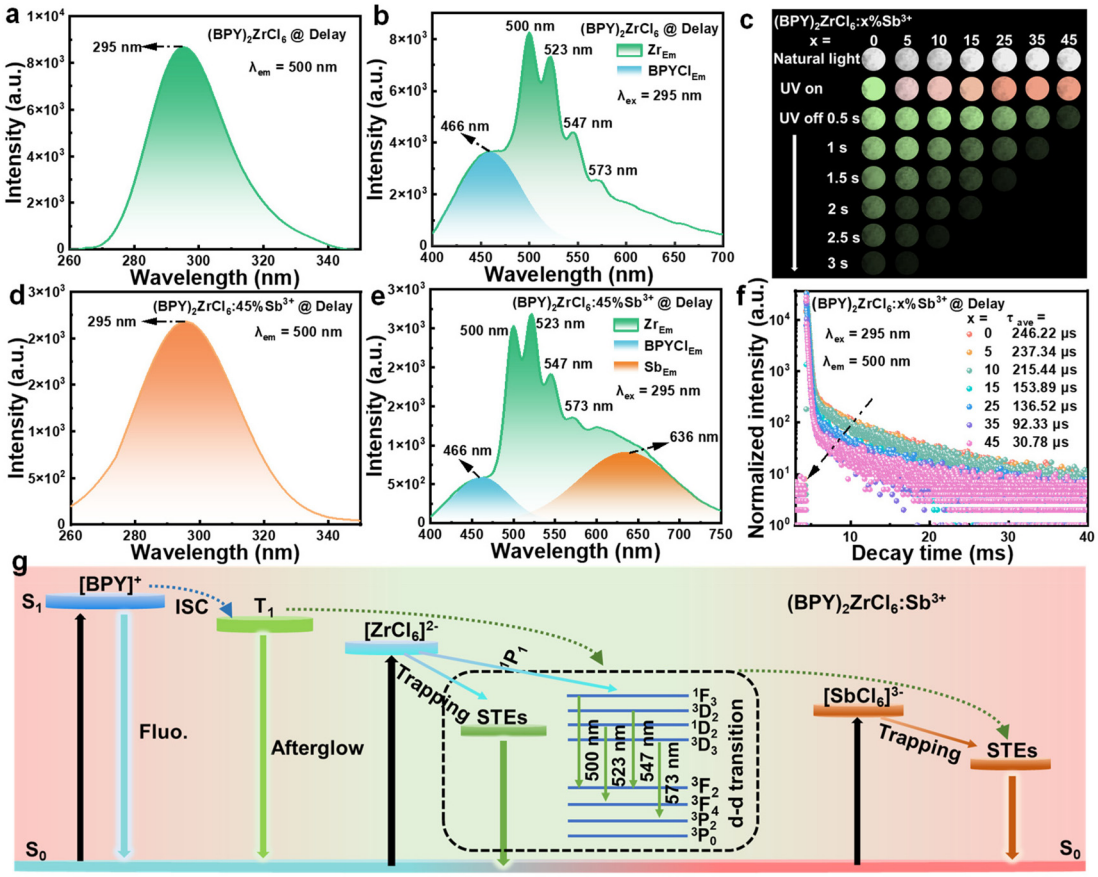

Fig. 3 (a and b) Delayed PLE/PL spectra of $(BPY)_2ZrCl_6$. (c) Photographs of patterns formed by $(BPY)_2ZrCl_6$:$x\%Sb^{3+}$ (x = 0–45) powders under daylight, 340 nm UV, and afterglow. (d and e) Delayed PLE/PL spectra of $(BPY)_2ZrCl_6$:$45\%Sb^{3+}$. (f) Delayed liftetime decay curves of $(BPY)_2ZrCl_6$:$x\%Sb^{3+}$ (x = 0–45) monitored at 500 nm. (g) Energy-level diagram illustrating exciton relaxation and transfer pathways in $(BPY)_2ZrCl_6$ and $(BPY)_2ZrCl_6$:Sb^{3+}. (Note: Fluo., fluorescence; ISC, inter-system crossing; T_1, triplet state; S_1, the lowest singlet state; S_0, ground state; STEs, self-trapped excitons.).

sion originates from the BPYCl triplet state. The four longer-wavelength peaks are assigned to d-d transitions of the $[ZrCl_6]^{2-}$ center, which are superimposed on the underlying broadband STEs emission of the same inorganic moiety.

Photographs recorded under daylight, 340 nm UV and afterglow conditions (Fig. 3c) visually corroborate the spectral trends: the undoped powder displays a bright green afterglow that remains visible for 3 s, whereas the $45\%Sb^{3+}$ sample fades within 0.5 s while retaining the same chromaticity. Upon introduction of Sb^{3+} (0–45%), the delayed excitation profile remains unchanged (Fig. 3d), implying that the primary absorption step is still dominated by the $[ZrCl_6]^{2-}$ chromophore. However, a new broadband centered at 636 nm emerges in the afterglow window (Fig. 3e), growing concomitantly with the decrease of the emission bands at 500, 523, 547, and 573 nm. Correspondingly, the integrated afterglow intensity drops by one order of magnitude (Fig. S16) and the lifetime monitored at 500 nm shortens from 246.22 μs (x = 0) to 30.78 μs (x = 45) under 295 nm pulsed excitation (Fig. 3f). The mono-exponential character of each decay indicates that a single kinetic population is quenched, consistent with Förster-type transfer from the $[ZrCl_6]^{2-}$ STEs to the $^3P_1$ level of $[SbCl_6]^{3-}$. The absence of a rise component at 636 nm further suggests that the transfer rate is fast compared with the intrinsic 500 nm lifetime.

The energy-level diagram (Fig. 3g) explains these observations. Photo-excitation promotes electrons to the singlet manifold of BPYCl (S_1). Inter-system crossing (ISC) channels a fraction to the T_1 state, whose energy is subsequently transferred to $[ZrCl_6]^{2-}$ and partially re-emitted as green afterglow. Sb^{3+} introduces a lower-lying acceptor level that competes for the same triplet reservoir. Consequently, the STEs population is drained before radiative recombination, and the afterglow duration is reduced to below the eye-detection limit at 45% Sb^{3+}. The retained afterglow, albeit weak, evidences that the $[SbCl_6]^{3-}$ center itself participates in a STEs-mediated down-conversion pathway, yet its radiative yield is suppressed by efficient non-radiative relaxation within the heavily distorted octahedron.

2.3. DFT-unravelled band alignment and site-selective exciton confinement in Sb^{3+}-incorporated $(BPY)_2ZrCl_6$

To elucidate the dual fluorescence-afterglow behavior, we first examined the intrinsic photophysics of the organic BPYCl.

Published on 18 März 2026. Downloaded on 05.06.2026 21:27:24.

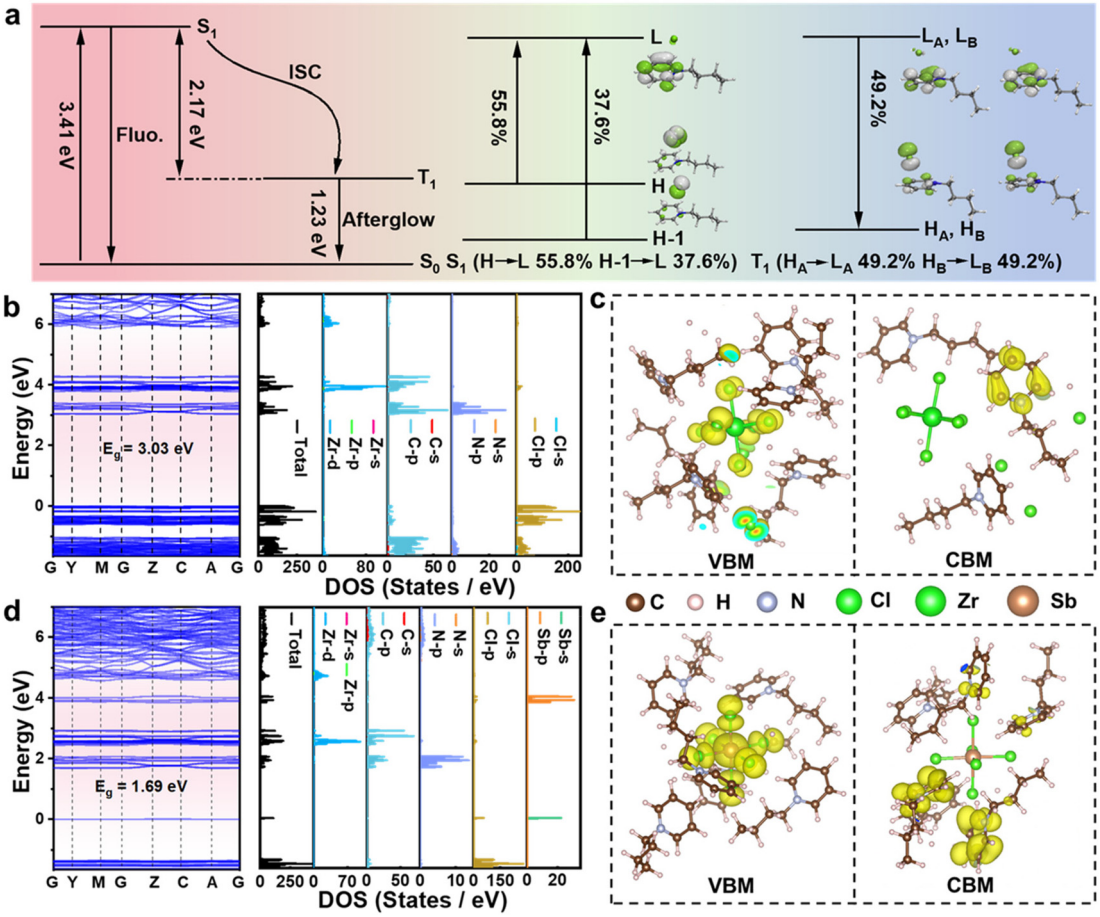

Fig. 4 (a) Energy-level diagram and transition mechanism of BPYCl. (b and c) The computed electronic band structure, density of states (DOS) and charge density distribution of the conduction band minimum (CBM) and the valence band maximum (VBM) for $(BPY)_2ZrCl_6$ crystals. (d and e) The computed electronic band structure, density of states (DOS) and charge density distribution of the conduction band minimum (CBM) and the valence band maximum (VBM) for $(BPY)_2ZrCl_6$:Sb^{3+} crystals.

First-principles calculations (Fig. 4a) reveal that photo-excitation promotes an electron to a higher-lying singlet state (3.41 eV), followed by rapid relaxation to S_1. From S_1, two primary pathways emerge: (i) radiative decay to S_0, generating fluorescence with a short lifetime, and (ii) ISC (energy gap 2.17 eV) to the metastable T_1 state. The spin-forbidden $T_1 \rightarrow S_0$ transition yields long-lived afterglow at 1.23 eV. The S_1 state is dominated by HOMO → LUMO (55.8%) and HOMO−1 → LUMO (37.6%) single-electron promotions, whereas the T_1 state lies 2.17 eV below S_1 and is principally described by $HOMO_A \rightarrow LUMO_A$ (49.2%) and $HOMO_B \rightarrow LUMO_B$ (49.2%).

DFT calculations reveal that the indirect band gap of pristine $(BPY)_2ZrCl_6$ is 3.03 eV (Fig. 4b). The valence-band maximum (VBM) is overwhelmingly comprised of Cl p orbitals that reside inside the $[ZrCl_6]^{2-}$ octahedra, whereas the conduction band bottom (CBM) is mainly contributed by the C p and N p orbitals confined within the BPYCl pyridine ring. This orbital allocation is corroborated by the charge density distribution plotted in Fig. 4c: the VBM density is confined within the inorganic framework, while the CBM density is concentrated on the organic π-system. Consequently, photo-excitation promotes an electron from a Cl-based orbital centered on $[ZrCl_6]^{2-}$ to a π* orbital centered on BPYCl, generating an intrinsic spatial separation of electron and hole across the organic–inorganic interface. Radiative recombination can therefore proceed along two competing pathways: (i) direct electron–hole recombination on the organic sublattice, yielding the 466 nm fluorescence/afterglow fingerprint of BPYCl, and (ii) lattice relaxation into STEs and d-d transitions within the distorted $[ZrCl_6]^{2-}$ cage. The calculated orbital origin and charge distribution thus provide a microscopic justification for the experimentally observed dual emission and explain why both organic and inorganic sub-lattices must be regarded as independent yet coupled luminophores in the title hybrid.

Upon incorporation of optically-active Sb^{3+}, the indirect band gap collapses from 3.03 eV to 1.69 eV (Fig. 4d), signaling a pronounced modification of the electronic structure. While the CBM is still constructed from C p and N p orbitals of the BPYCl, the VBM is now dominated by Sb s and Cl p states (Fig. 4e), a clear signature of the formal $[ZrCl_6]^{2-} \rightarrow [SbCl_6]^{3-}$ substitution. Charge-density analysis further reveals that the CBM electron density is spatially confined inside the distorted

 This journal is © the Partner Organisations 2026

Published on 18 März 2026. Downloaded on 05.06.2026 21:27:24.

$[SbCl_6]^{3-}$ octahedron. Such spatial separation of electron and hole states is favorable for the formation of Sb^{3+}-centered STEs under UV excitation, because the localized wavefunctions efficiently stabilize lattice distortions that trap the exciton.[41]

Spin-polarized calculations (Fig. S17) indicate that the undoped host possesses perfectly compensated spin-up and spin-down populations, whereas the doped system carries one excess spin-up electron, concomitantly, the Sb site is deficient in one spin-down electron, shifting the minority-spin states toward higher energy. This imbalance generates empty levels adjacent to the valence band that can accept thermally excited electrons, a configuration consistent with p-type semiconduction. Experimentally, diffuse-reflectance spectra yield indirect gaps of 3.11 eV and 1.99 eV for the undoped and doped solids, respectively (Fig. S18), in satisfactory agreement with the computed values. Thus, the DFT results elucidate the emission mechanism: in the pristine crystal, radiative decay arises from both the $S_1 \rightarrow S_0$ fluorescence and $T_1 \rightarrow S_0$ afterglow of BPYCl, augmented by STEs and d-d transitions within $[ZrCl_6]^{2-}$. After Sb^{3+} substitution, the $[SbCl_6]^{3-}$ moiety dominates the VBM, narrows the gap to 1.69 eV, and localizes the lowest excitons on the antimony site, thereby giving rise to the STEs emission.

2.4. Thermal, ambient, and electron–phonon robustness of $(BPY)_2ZrCl_6:Sb^{3+}$

The thermal and ambient stability of the crystals were investigated. Thermogravimetric analysis determined the decomposition temperatures of $(BPY)_2ZrCl_6$ and $(BPY)_2ZrCl_6:Sb^{3+}$ to be 270 °C and 310 °C, respectively (Fig. 5a). The higher decomposition temperature indicates that Sb^{3+} doping enhances the thermal stability of the host material.[42] Such high thermal robustness suggests its capability to withstand heat generated during prolonged operation, making it a potential candidate for optoelectronic applications.

Ambient-stability tests were conducted without encapsulation. After 60 days in air, the powder X-ray diffraction patterns remained indistinguishable from those of the fresh sample (Fig. S19). Concurrently, the PLQYs decreased only marginally from 83.2% to 80.2%, and the integrated emission intensity retained 91% of its initial value (Fig. S20). These results demonstrate effective moisture resistance of the material, with the PLQYs retaining 96% of its initial value after 60 days in air.

Temperature-dependent PL from 313 to 443 K (under 340 nm excitation) showed reversible quenching of both the 480 nm and 616 nm bands (Fig. 5b and c). A single heating–cooling cycle recovered 94% of the initial intensity (Fig. S21), confirming the absence of thermally activated defect formation. From 77 K upward (Fig. 5d), both emission bands widened and blue-shifted, consistent with the behavior of emission dominated by electron–phonon coupling.[43,44] The Huang–Rhys factor (S), a measure of the electron–phonon coupling strength, was derived from the temperature-dependent spectral linewidth (FWHM, 77–298 K) using eqn (2):[45–47]

$$\mathrm{FWHM}(T) = 2.36\hbar\omega_{\mathrm{phonon}}\sqrt{S\coth\left(\frac{\hbar\omega_{\mathrm{phonon}}}{2kT}\right)} \qquad (2)$$

where T is the temperature, S is Huang–Rhys factor, $\hbar\omega_{\mathrm{phonon}}$ is the phonon frequency, and k is the Boltzmann constant. The

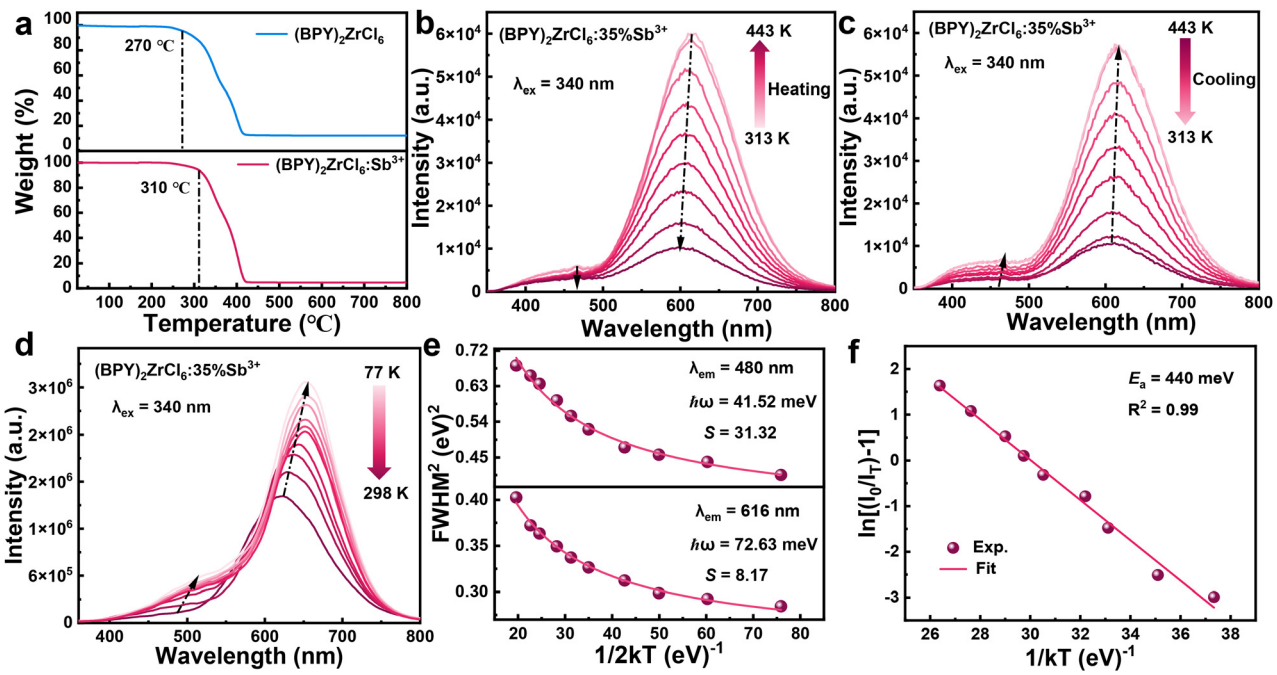

Fig. 5 (a) TGA curves of $(BPY)_2ZrCl_6$ and $(BPY)_2ZrCl_6:Sb^{3+}$. (b and c) Temperature-dependent PL spectra of $(BPY)_2ZrCl_6$:35%Sb^{3+} during the processes of heating and cooling under 340 nm excitation. (d) Integrated PL intensity *versus* temperature 77–298 K. (e) FWHM *versus* temperature used to extract Huang–Rhys factor and (f) Arrhenius fit of integrated intensity yielding activation energy of $(BPY)_2ZrCl_6$:35%Sb^{3+} crystal.

Published on 18 März 2026. Downloaded on 05.06.2026 21:27:24.

calculation yields S = 31.32 for the 480 nm band and 8.17 for the 616 nm band, with effective phonon frequencies of 41.52 and 72.63 meV, respectively (Fig. 5e). These exceptionally large S values place the emission deep in the strong-coupling regime and explain the remarkable Stokes shifts observed experimentally. The data for $(BPY)_2ZrCl_6$:35%Sb^{3+} were fitted with the Arrhenius-type quenching model,[48,49]

$$I(T) = I_0/(1 + A\exp^{-E_a/k_B T}) \quad (3)$$

where I_0 is the integrated intensity at 0 K and A is a constant. Fig. 5f shows that the E_a of $(BPY)_2ZrCl_6$:35%Sb^{3+} is 440 meV, which is much higher than the thermal energy at room temperature (26 meV). The large S value combined with the high activation energy indicate that the low-energy emissions at 480 nm and 616 nm originate from highly localized states. This strong localization enables STEs to resist thermal quenching and form stable, thermally robust emissive centers.[50]

2.5 Dual-mode solid-state lighting and time-resolved cryptography enabled by a single-component $(BPY)_2ZrCl_6:Sb^{3+}$ phosphor

One-component conversion layers were fabricated by dispensing $(BPY)_2ZrCl_6$:x%Sb^{3+} powders (x = 5, 10) onto 310 nm UV chips, and the resulting devices delivered bright cold-white and warm-white emission, respectively (Fig. 6a and b). Under these illuminants, a standard color target exhibited high color saturation and vividness (Fig. 6c), confirming that the continuous spectrum spanning 466 nm and 616 nm is able to furnish good color rendition. Electroluminescence (EL) spectra recorded for x = 5 and x = 10 revealed that the relative weight of the 466 nm and 616 nm components can be tuned simply by adjusting the Sb^{3+} content, thereby permitting chromaticity engineering without altering the host lattice (Fig. S22). Consequently, CIE chromaticity coordinates of (0.2900, 0.2956) and (0.3623, 0.3376), color-rendering indices (CRI) of 96 and 93, and correlated color temperatures (CCT) of 8714 K and 4268 K were obtained for the two doping levels, values that fall squarely within the cold- and warm-white specification windows.

Operation stability was examined by ramping the forward current from 15 to 90 mA (Fig. S23). Emission intensity increased linearly with drive current, yet neither peak position nor spectral shape exhibited any discernible shift, underscoring the absence of thermal droop or re-absorption effects. Moreover, CRI and CCT remained essentially constant across the entire current envelope (Fig. S24). Long-term stability of the WLEDs was evaluated under continuous operation

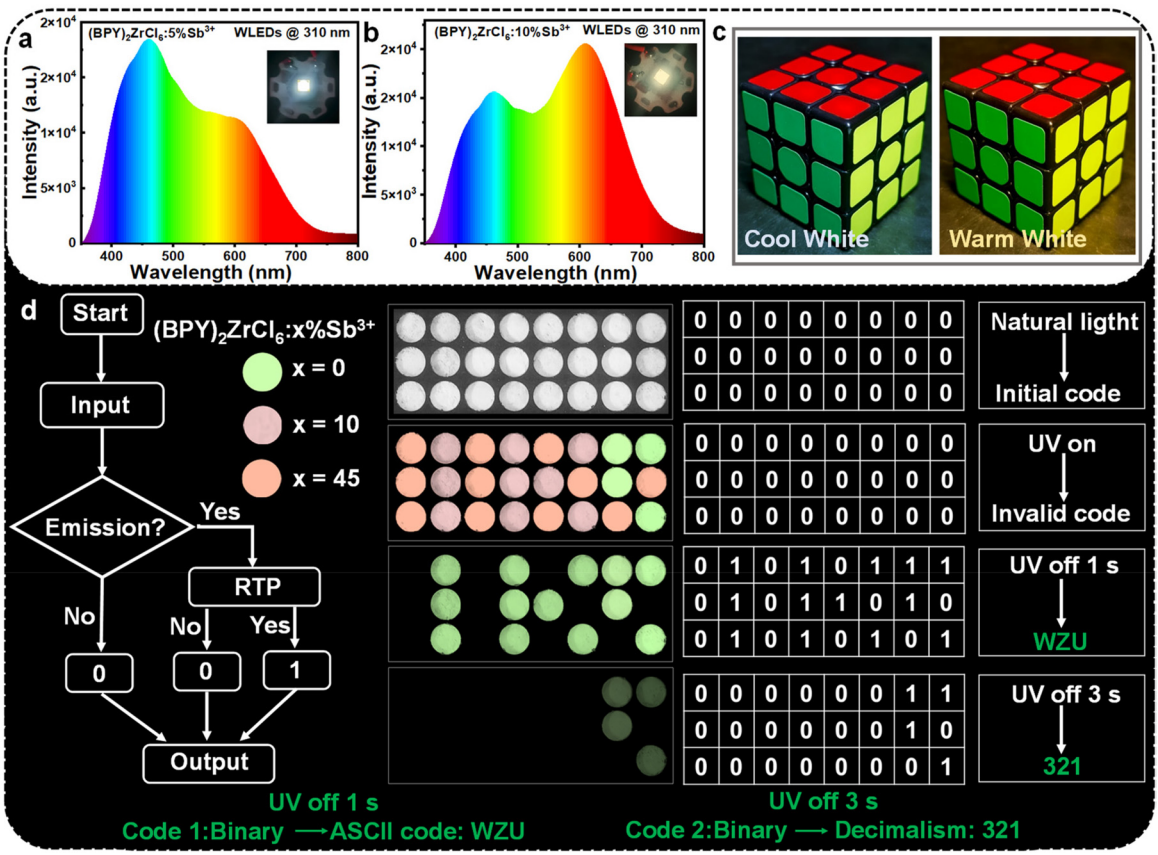

Fig. 6 (a and b) EL spectra of WLEDs (310 nm chip) coated with $(BPY)_2ZrCl_6$:x%Sb^{3+} (x = 5, 10): insets show operating devices. (c) The color performance of magic cube under WLEDs irradiation. (d) Time-resolved encryption/decryption schematic and dot-matrix evolution photographs.

 This journal is © the Partner Organisations 2026

Published on 18 März 2026. Downloaded on 05.06.2026 21:27:24.

(Fig. S25). After 100 h, the CRI of $(BPY)_2ZrCl_6$:5%Sb^{3+} WLEDs decreased slightly from 96 to 85 and the CCT shifted upward by about 3%. The CRI of $(BPY)_2ZrCl_6$:10%Sb^{3+} WLEDs decreased slightly from 93 to 84 and the CCT shifted upward by about 4%. These data indicate that the performance of the WLEDs devices does not undergo significant changes during long-term operation. Accordingly, this Sb^{3+}-tunable hybrid is regarded as a promising candidate for next-generation solid-state lighting applications that demand high color quality and simplified device architecture.

The distinct fluorescence-afterglow sequences of undoped and Sb^{3+}-doped $(BPY)_2ZrCl_6$ were exploited to design an ASCII-based, dual-step encryption protocol. In the adopted logic, the occurrence of a persistent afterglow following 340 nm excitation is defined as "1", and its non-occurrence is defined as "0". Under natural light, patterns printed with $(BPY)_2ZrCl_6$:x% Sb^{3+} (x = 0, 10, 45) powders appear colorless and disclose no information (Fig. 6d). Upon continuous UV illumination the same arrays merely exhibit bright green, pale-pink and orange-red emission that still masks the encoded message. Only when a time-resolved detector is triggered 1 s after switch-off is the first 8-bit string resolved, translating into the ASCII word "WZU". Extending the delay to 3 s produces a second 8-bit block that is converted into the decimal number "321". Concatenation of the two time-gated readouts finally yields the unique signature "WZU 321". Because the afterglow lifetime can be continuously tuned by the Sb^{3+} content, the temporal window for each bit is user-definable and virtually impossible to replicate without exact knowledge of the dopant level. Consequently, $(BPY)_2ZrCl_6$ and its Sb^{3+}-tailored derivatives provide a dynamic, multi-level anti-counterfeiting platform that offers a new route for high-security information protection.

3. Conclusions

In summary, a series of Sb^{3+}-doped 0D OIHP, $(BPY)_2ZrCl_6$:x% Sb^{3+} (0–45), were successfully synthesized *via* a hydrothermal method. The material exhibits multi-center emission: 466 nm emission originating from the organic molecule BPYCl, as well as STEs emission and d–d transitions (500, 523, 547, 573 nm) from the inorganic $[ZrCl_6]^{2-}$octahedra. Introducing Sb^{3+} establishes an efficient energy-transfer pathway from the host to the $[SbCl_6]^{3-}$ dopant sites, which enables tunable white-light emission and reduces the afterglow lifetime. DFT calculations elucidated the source of the afterglow, confirmed that doping caused band gap collapse (3.03 → 1.69 eV) and valence band reconstruction, promoting the formation of Sb center STEs. This material showed a PLQYs of 83.2%, good thermal stability, and effective moisture resistance. The dual-mode luminescence and tunable afterglow properties demonstrated here suggest the potential of such single-component materials for integrated applications in efficient solid-state lighting and dynamic information encryption.

Conflicts of interest

The authors declare no conflict of interest.

Data availability

The data supporting the findings of this study are openly available upon request from the corresponding author, Yuexiao Pan, at yxpan@wzu.edu.cn. Data will be shared promptly, subject to no privacy or proprietary restrictions.

For access to the data, interested parties should submit a brief request outlining the specific data needed and their research purpose. The authors will review and respond to requests within a reasonable timeframe.

For any inquiries regarding data availability, please contact the corresponding author.

Supplementary information (SI) is available. See DOI: **https://doi.org/10.1039/d5qi02511g**.

CCDC 2454281 contains the supplementary crystallographic data for this paper.[51]

Acknowledgements

This research is financially supported by National Natural Science Foundation (NSF) of China (12504468, 52172152, 52172166), and the Guangdong Basic and Applied Basic Research Foundation (No. 2024A1515110123).

References

1 Y. J. Zhao, X. R. Yang, L. Yang, F. J. Xing, C. H. Liu, Y. S. Di, G. Y. Cao, S. B. Wei, X. F. Yang, X. W. Zhang, Y. S. Liu and Z. X. Gan, Advanced Optical Information Encryption Enabled by Polychromatic and Stimuli-Responsive Luminescence of Sb-Doped Double Perovskites, *Adv. Sci.*, 2024, **11**, 2308390.

2 Z. Chen, Z. S. L. Ruan, S. L. Jiang, Q. Zhang and Y. Luo, High-Security and High-Efficiency Information Encryption/Decryption Based on 2D Hybrid Organic-Inorganic Perovskites via Delicate Organic-Cation Engineering, *Angew. Chem., Int. Ed.*, 2025, **64**, e202504327.

3 Y. Kou, Z. X. Yang, G. Y. Tan, L. J. Liang, H. R. Cheng, P. R. Su and Y. Tang, Yb^{3+}-Complex-Mediated Assembly of $CsPbBr_3$ Nanocrystals Enables Multilevel Optical Encryption, *Adv. Funct. Mater.*, 2025, e18377.

4 X. K. Li, X. Y. Qiu, X. Yang, P. Zhou, Q. Q. Guo and X. X. Zhang, Multi-Modal Melt-Processing of Birefringent Cellulosic Materials for Eco-Friendly Anti-Counterfeiting, *Adv. Mater.*, 2024, 2407170.

5 A. K. Singh, S. Singh and B. K. Gupta, Highly-Efficient, Chemically-Stable, UV/Blue Light Excitable Biluminescent Security Ink to Combat Counterfeiting, *ACS Appl. Mater. Interfaces*, 2018, **10**, 44570–44575.

Published on 18 März 2026. Downloaded on 05.06.2026 21:27:24.

6 J. J. Wang, C. Chen, W. G. Chen, J. S. Yao, J. N. Yang, K. H. Wang, Y. C. Yin, M. M. Yao, L. Z. Feng, C. Ma, F. J. Fan and H. B. Yao, Highly Luminescent Copper Iodide Cluster Based Inks with Photoluminescence Quantum Efficiency Exceeding 98%, *J. Am. Chem. Soc.*, 2020, **142**, 3686–3690.

7 J. H. Wei, W. T. Ou, J. B. Luo and D. B. Kuang, Zero-Dimensional Zn-Based Halides with Ultra-Long Room-Temperature Phosphorescence for Time-Resolved Anti-Counterfeiting, *Angew. Chem., Int. Ed.*, 2022, **61**, e202207985.

8 J. Li, J. J. Wu, Y. H. Xiao, L. S. Rao, R. S. Zeng, K. Xu, X. C. Huang, J. Z. Zhang and B. B. Luo, Efficient Triplet Energy Transfer in a 0D Metal Halide Hybrid with Long Persistence Room-Temperature Phosphorescence for Time-Resolved Anti-Counterfeiting, *Inorg. Chem. Front.*, 2023, **10**, 7167.

9 J. Y. Zhou, D. P. Liu, L. Q. Li, M. Qi, G. Q. Yin and T. Chen, Responsive Organic Room-Temperature Phosphorescence Materials for Spatial-Time-Resolved Anti-Counterfeiting, *Chin. Chem. Lett.*, 2024, **35**, 109929.

10 X. Zhang, J. X. Hao, M. L. Cai, B. Zhang, X. M. Zhen and Y. Wu, Spatial & Temporal Dual-Resolved Anti-Counterfeiting Applications in a Long Afterglow System Based on Bismuth Halides, *Inorg. Chem.*, 2025, **64**, 8238–8249.

11 T. H. Chen, Y. J. Ma and D. P. Yan, Single-Component 0D Metal-Organic Halides with Color-Variable Long-Afterglow toward Multi-Level Information Security and White-Light LED, *Adv. Funct. Mater.*, 2023, **33**, 2214962.

12 X. T. Shen, M. H. Li, Q. S. Liu, H. Y. Hu and L. L. Zhang, Water-Resistant $SrAl_2O_4$:Eu^{2+}, Dy^{3+} Phosphor with Extended Afterglow Duration, *Adv. Funct. Mater.*, 2025, e15541.

13 S. Z. Zhang, Y. Ding, Z. X. Li, K. R. Qiang, C. H. Wang, N. Han, M. J. Liu and J. S. Zhong, Multimode Emission from Bi^{3+} Induced Oxygen Vacancy Engineering in Spinel-Type Phosphor for Versatile Optical Applications, *Chem. Eng. J.*, 2025, **524**, 168952.

14 Z. H. Deng, F. C. Kong, Z. Q. Deng, J. M. Zhou, S. Y. Yang, S. He, J. Y. Zhang, Y. F. Zuo, J. Wang, X. M. Chen, R. T. K. Kwok, G. C. Jia, P. C. Y. Chow, D. L. Phillips, P. Alam, J. W. Y. Lam and B. Z. Tang, Visualizing Triplet Energy Transfer in Organic Near-Infrared Phosphorescent Host-Guest Materials, *Angew. Chem., Int. Ed.*, 2024, **63**, e202412182.

15 W. W. Xie, W. B. Huang, J. T. Li, Z. K. He, G. X. Huang, B. S. Li and B. Z. Tang, Anti-Kasha Triplet Energy Transfer and Excitation Wavelength Dependent Persistent Luminescence from Host-Guest Doping Systems, *Nat. Commun.*, 2023, **14**, 8098.

16 F. X. Lin, H. Y. Wang, Y. F. Cao, R. J. Yu, G. D. Liang, H. H. Huang, Y. X. Mu, Z. Y. Yang and Z. G. Chi, Stepwise Energy Transfer: Near-Infrared Persistent Luminescence from Doped Polymeric Systems, *Adv. Mater.*, 2022, **34**, 2108333.

17 H. J. Wang, Y. T. Li, M. C. Shao, C. S. Yu, J. Y. Yang, L. Y. Liu, S. N. Wang and J. M. Dou, Phototunable Phosphorescence Energy Transfer Based on Photodimerization of Coumarin-12-Crown-4 Accelerated by γ-Cyclodextrin, *Chem. Eng. J.*, 2025, **504**, 158772.

18 S. S. Chen, Y. Liu, Y. Zhang, D. J. Zhang, Z. F. Chen, D. L. Wang, K. W. Wu, Y. Xiong and B. Z. Tang, Ultralong Room-Temperature Phosphorescence Achieved by Microcapsule Rupture-Triggered *In situ* Polymerization for High-Contrast Damage Visualization and Advanced Anti-Counterfeiting, *Adv. Mater.*, 2025, e14584.

19 Z. R. Hua, W. M. Sun, Y. Tian and H. B. Fu, Modulating Room-Temperature Phosphorescence Emission of Piperonylamine-Based Organic Inorganic Hybrids via Metallic Halide, *Adv. Opt. Mater.*, 2025, **13**, 2500414.

20 S. Y. Liu, X. Y. Fang, B. Lu and D. P. Yan, Wide Range Zero-Thermal-Quenching Ultralong Phosphorescence from Zero-Dimensional Metal Halide Hybrids, *Nat. Commun.*, 2020, **11**, 4649.

21 X. Han, P. X. Cheng, R. C. Shi, Y. S. Zheng, S. M. Qi, J. L. Xu and X. H. Bu, Linear Optical Afterglow and Nonlinear Optical Harmonic Generation from Chiral Tin (IV) Halides: the Role of Lattice Distortions, *Mater. Horiz.*, 2023, **10**, 1005–1011.

22 G. J. Zhou, Y. L. Mao, J. Zhang, Q. Q. Ren, M. Molokeev, Z. G. Xia and X. M. Zhang, Dynamic Phosphorescence/Fluorescence Switching in Hybrid Metal Halides Toward Time-Resolved Multi-Level Anti-Counterfeiting, *Adv. Funct. Mater.*, 2025, **35**, 2413524.

23 M. Ren, S. Zhang, J. Wu, Q. S. Hu, S. Cao, B. S. Zou, Z. X. Yin, W. W. Yu and R. S. Zeng, Engineered Energy Transfer in Room-Temperature Phosphorescent Materials for Time-Resolved Dual-Mode Encryption, *Adv. Funct. Mater.*, 2025, **35**, 2420362.

24 Z. S. Luo, Y. J. Liu, Y. L. Liu, C. Li, Y. W. Li, Q. Li, Y. Wei, L. M. Zhang, B. Xu, X. Y. Chang and Z. W. Quan, Integrated Afterglow and Self-Trapped Exciton Emissions in Hybrid Metal Halides for Anti-Counterfeiting Applications, *Adv. Mater.*, 2022, **34**, 2200607.

25 S. W. Feng, Y. J. Ma, S. Q. Wang, S. S. Gao, Q. Q. Huang, H. Y. Zhen, D. P. Yan, Q. D. Ling and Z. H. Lin, Light/Force-Sensitive 0D Lead-Free Perovskites: From Highly Efficient Blue Afterglow to White Phosphorescence with Near-Unity Quantum Efficiency, *Angew. Chem., Int. Ed.*, 2022, **61**, e202116511.

26 Z. L. Li, M. Y. Cao, Z. H. Rao, X. J. Zhao and X. Gong, Tunable Afterglow and Self-Trapped Exciton Emissions in Zr(IV)-Based Organic-Inorganic Metal Halide Hybrids by Metal-Ion Doping, *Small*, 2023, **19**, 2302357.

27 G. K. Dai, Z. M. Ma, Y. X. Qiu, Z. W. Li, X. H. Fu, H. Jiang and Z. Y. Ma, Excitation-Dependent Luminescence of 0D $((CH_3)_4N)_2ZrCl_6$ across the Full Visible Region, *J. Phys. Chem. Lett.*, 2022, **13**, 7553–7560.

28 B. Chen, Y. Guo, Y. Wang, Z. Liu, Q. Wei, S. X. Wang, A. L. Rogach, G. C. Xing, P. Shi and F. Wang, Multiexcitonic

 This journal is © the Partner Organisations 2026

Published on 18 März 2026. Downloaded on 05.06.2026 21:27:24.

Emission in Zero-Dimensional Cs_2ZrCl_6:Sb^{3+} Perovskite Crystals, *J. Am. Chem. Soc.*, 2021, **143**, 17599–17606.

29 X. Y. Yun, J. H. Nie, H. Q. Wang, H. L. Hu, H. Z. Zhong, D. H. Xu, Y. M. Shi and H. N. Li, Multiexcitonic Emission of Organic-Inorganic $(C_4H_{12}N)_2ZrCl_6$:Sb^{3+} Perovskites across the Full Visible Region for Anticounterfeiting Applications, *ACS Appl. Nano Mater.*, 2023, **6**, 19581–19587.

30 Y. M. Tang, G. Q. Pu, C. B. Kang, L. J. Liu, D. Xu, W. Chen, H. Bi and J. C. Wang, Ultrabroadband Tunable Emission in Hybrid Zr-perovskite via Sb^{3+} Doping: Harnessing Singlet-Triplet Energy Transfer and Self-Trapped Excitons, *Mater. Today Phys.*, 2025, **57**, 101810.

31 Y. Zha, Q. D. Duan, F. J. Meng, D. C. Zhou, J. Han, Y. G. Wen and J. B. Qiu, Singlet-Triplet Emissive Tuning Enables Dual-Mode Stimuli-Responsive Luminescence in 0D Cs_2ZrCl_6:Sb^{3+}/8-Hydroxyquinoline Composites for Multilevel Optical Encryption, *Chem. Eng. J.*, 2025, **503**, 158508.

32 H. Wang, S. Zhan and Z. G. Xia, Composition Modulation of Cs_2ZrCl_6-based Scintillator Film via Vapor Deposition for Large-Area X-Ray Imaging, *Small Methods*, 2025, **9**, 2500273.

33 H. W. Li, K. Han, Z. Y. Li, H. X. Yue, X. Y. Fu, X. Y. Wang, Z. G. Xia, S. Y. Song, J. Feng and H. J. Zhang, Multiple Energy Transfer Channels in Rare Earth Doped Multi-Exciton Emissive Perovskites, *Adv. Sci.*, 2023, **11**, 2307354.

34 H. Peng, W. Tian, Q. L. Wei, L. H. Kong, G. Dai, J. L. Zhao and B. S. Zou, Component/Stimulus-Dependent Multi-Exciton Emission in Zr(IV)-Based Organic Metal Halides Triggered by Supramolecular Assembly and Antimony Doping, *Laser Photonics Rev.*, 2025, **19**, 2401724.

35 J. Reader and M. D. Lindsay, Spectrum and Energy Levels of Five-Times Ionized Zirconium (Zr VI), *Phys. Scr.*, 2016, **91**, 025401.

36 X. Y. Liu, X. Xu, B. Li, L. L. Yang, Q. Li, H. Jiang and D. S. Xu, Tunable Dual-Emission in Monodispersed Sb^{3+}/Mn^{2+} Codoped $Cs_2NaInCl_6$ Perovskite Nanocrystals through an Energy Transfer Process, *Small*, 2020, **16**, 2002547.

37 J. H. Nie, B. Zhou, S. F. Fang, H. Z. Zhong, H. N. Li and Y. M. Shi, Efficient Multicolor and White Photoluminescence in Erbium- and Holmium-Incorporated $Cs_2NaInCl_6$:Sb^{3+} Double Perovskites, *Chem. Mater.*, 2022, **34**, 6288–6295.

38 H. Wang, Y. X. Pan, Y. H. Ding, H. Z. Lian, J. Lin and L. Y. Li, Tunable Multicolor Emission and High Thermal Stability in Single-Matrix Luminescent Crystals Based on Calcium Perovskites for Advanced Solid-State Lighting Applications, *Adv. Opt. Mater.*, 2024, **12**, 2400935.

39 Z. W. Lu, S. Chen, Y. F. Liu, C. X. Yuan, R. Y. Li, P. Sun, Z. H. Luo, Z. H. Liu and J. Jiang, $LiGaP_2O_7$:Cr^{3+}, Yb^{3+} Phosphors for Broadband NIR LEDs toward Multiple Applications, *J. Alloys Compd.*, 2023, **956**, 170311.

40 C. B. Xu, J. N. Zhang, Y. X. Pan, Y. Y. Liu, X. Y. Yang, H. P. Xiao and J. Zou, Dual Emission and Efficient Energy Transfer in $(4\text{-BTP})_2ZnBr_4$:Mn^{2+} for Enhanced Optical Properties, *Mater. Today Chem.*, 2025, **49**, 102975.

41 Y. S. Xu, R. J. Yang, Q. D. Duan, Z. B. Deng, T. Y. Guo, M. H. Su, X. C. Ning, Y. G. Yang, Y. Zha, D. C. Zhou, Y. Yang, Q. Wang, Y. G. Wen and J. B. Qiu, Tailoring Self-Trapped Exciton Emission in 0D Indium-Based Perovskites by Solvent-Induced Crystal Structure Engineering, *Laser Photonics Rev.*, 2025, **19**, 2500005.

42 J. Kim, S. W. Park, Y. Lee, H. Hosono, B. Park and J. Kim, Synthesis of Stable Iodoplumbate and Perovskite for Efficient Annealing-Free Device and Long-Term Storage, *SusMat*, 2023, **3**, 821–833.

43 X. Y. Song, X. S. Liu, D. W. Zhang, J. Y. Liao, S. Q. Zhu and W. Zheng, High-Contrast Thermochromism in Room-Temperature Transparent Layered Perovskite PEA_2PbBr_4 with a High Temperature-Induced Bandgap Change Rate of 0.8 meV/K, *J. Am. Chem. Soc.*, 2024, **146**, 24670–24680.

44 F. Ahmad, M. Lassoued, Q. C. Luo, Y. N. Shen, L. H. Yan and Y. Z. Zheng, Site Specific In^{3+}-Alloying Unlocks Intense Photoluminescence and High Stability in Antimony Halide Hybrids for WLED and Anticounterfeiting Applications, *Adv. Mater.*, 2025, **29**, 2418435.

45 K. Han, X. S. Wang, J. C. Jin, S. Zhang, L. Li, Y. Z. Wang, L. X. Ning and Z. G. Xia, Suppressing Electron-Phonon Coupling for Narrow-Band Emitting Eu(II)-Based Perovskitoids, *Nat. Commun.*, 2025, **16**, 5641.

46 Y. Liu, Y. Wu, A. Sokolova, X. M. Shi, S. V. Kershaw, Y. S. Wu, L. Polavarapu, X. M. Li and A. L. Rogach, Photoluminescence of Te-Doped Double Perovskite Cs_2ZrCl_6 Nanocrystals Versus Bulk: Insights from Temperature-Dependent Spectroscopy, *Small*, 2025, **21**, 2501342.

47 Z. Tang, R. Z. Liu, J. S. Chen, D. Y. Zheng, P. W. Zhou, S. P. Liu, T. X. Bai, K. B. Zheng, K. L. Han and B. Yang, Highly Efficient and Ultralong Afterglow Emission with Anti-Thermal Quenching from $CsCdCl_3$:Mn Perovskite Single Crystals, *Angew. Chem., Int. Ed.*, 2022, **61**, e202210975.

48 C. Sun, C. Q. Jing, D. Y. Li, M. H. Dong, M. X. An, Z. H. Zhang, C. Y. Yue, H. H. Fei and X. W. Lei, In Situ Halide Vacancy Tuning of Low-Dimensional Lead Perovskites to Realize Multiple Adjustable Luminescence Performance, *Adv. Sci.*, 2025, **12**, 2412459.

49 M. H. Yang, W. Y. Ge, K. Matsumoto, M. Saruyama, R. Sato, H. Takekuma, R. Takahata and T. Teranishi, Reversible "on–off" Conversion and Ultra-high Temperature Sensitivity of a Zero-Dimensional Lead-Free $Cs_2InBr_5(H_2O)$:Sb^{3+} perovskite, *Inorg. Chem. Front.*, 2024, **11**, 5536.

50 X. Han, P. X. Cheng, S. S. Han, Z. H. Wang, J. J. Guan, W. Q. Han, R. C. Shi, S. H. Chen, Y. S. Zheng, J. L. Xu and X. H. Bu, Multi-Stimuli-Responsive Luminescence Enabled by Crown Ether Anchored Chiral Antimony Halide Phosphors, *Chem. Sci.*, 2024, **15**, 3530–3538.

51 CCDC 2454281: Experimental Crystal Structure Determination, 2026, DOI: **10.5517/ccdc.csd.cc2ncwc9**.